Available online at www.sciencedirect.com
SCIENCE DIRECT®
European Journal of Mechanics B/Fluids 24 (2005) 522–538

Experimental evaluation of numerical simulation of cavitating flow around hydrofoil

Matevž Dular [a,*], Rudolf Bachert [a], Bernd Stoffel [a], Brane Širok [b]

[a] *Laboratory for Turbomachinery and Fluid Power, Darmstadt University of Technology, Magdalenenstr. 4, 64289 Darmstadt, Germany*
[b] *Laboratory for Water and Turbine Maschines, University of Ljubljana, Askerceva 6, 1000 Ljubljana, Slovenia*

Received 8 June 2004; received in revised form 20 August 2004; accepted 28 October 2004

Available online 13 December 2004

Abstract

Cavitation in hydraulic machines causes different problems that can be related to its unsteady nature. An experimental and numerical study of developed cavitating flow was performed. Until now simulations of cavitating flow were limited to the self developed "in house" CFD codes. The goal of the work was to experimentally evaluate the capabilities of a commercial CFD code (Fluent) for simulation of a developed cavitating flow. Two simple hydrofoils that feature some 3D effects of cavitation were used for the experiments. A relatively new technique where PIV method combined with LIF technique was used to experimentally determine the instantaneous and average velocity and void ratio fields (cavity shapes) around the hydrofoils. Distribution of static pressure on the hydrofoil surface was determined. For the numerical simulation of cavitating flow a bubble dynamics cavitation model was used to describe the generation and evaporation of vapour phase. An unsteady RANS 3D simulation was performed. Comparison between numerical and experimental results shows good correlation. The distribution and size of vapour structures and the velocity fields agree well. The distribution of pressure on the hydrofoil surface is correctly predicted. The numerically predicted shedding frequencies are in fair agreement with the experimental data.

Keywords: Cavitation; Single hydrofoil; Visualization; PIV-LIV method; CFD

1. Introduction

Occurrence of cavitation in hydraulic machines leads to problems like vibration, increase of hydrodynamic drag, pressure pulsation, changes in flow kinematics, noise and erosion of solid surfaces. Most of these problems are related to transient behaviour of cavitation structures. For example Sirok et al. [1] showed that cavitation erosion is strongly related to unsteady fluctuations of the cavitation zone. Hence a study of unsteady cavitation behaviour is essential for a good prediction of above mentioned problems. To investigate the cavitation phenomenon and to validate numerical procedures, different investigations

* Corresponding author.
E-mail addresses: dular@tfa.maschinenbau.tu-darmstadt.de,matevz.dular@email.si (M. Dular), rbachert@tfa.maschinenbau.tu-darmstadt.de (R. Bachert), stoffel@tfa.maschinenbau.tu-darmstadt.de (B. Stoffel), brane.sirok@fs.uni-lj.si (B. Širok).

0997-7546/$ – see front matter
doi:10.1016/j.euromechflu.2004.10.004

Nomenclature

C_e	empirical constant	R_c	vapour condensation source term
C_c	empirical constant	T_∞	system temperature
F	force	v	velocity
f_g	gas mass fraction	v_m	mixture velocity
f_v	vapour mass fraction	ε	turbulence dissipation rate
g	gravitational acceleration	γ	liquid surface tension
k	turbulence kinetic energy	μ_m	mixture viscosity
n	exponent	μ_t	turbulent viscosity
p	pressure	ρ	density
p_{ref}	reference pressure	ρ_l	liquid density
p_v	vapour pressure	ρ_m	mixture density
p_∞	system pressure	ρ_v	vapour density
R_e	vapour generation source term	σ	cavitation number

were performed in the past (for example Stutz and Reboud [2], Stutz and Reboud [3]). With aid of the probe measurements (described in above mentioned investigations) the velocity can be measured only in one point at the time, hence only an average velocity field can be determined. An instantaneous distribution of the velocity in the whole region of interest is therefore impossible to obtain. The problem can be solved by PIV (Particle Image Vecilometry) technique as Zhang et al. [4] first showed. They employed PIV method to examine the turbulent flow in the wake of an open partial cavity. Both mean and fluctuating velocity components of the flow in the nozzle were measured, but only for the attached cavitation condition where vapour cloud separation does not occur and re-entrant jet is not present. Recently Laberteaux and Ceccio ([5] and [6]) upgraded the work of Zhang et al. [4] to the developed cavitating flow with vapour cloud separation and have also used different hydrofoils to obtain some 3-dimensional effects. However they were unable to obtain the information about the velocity field inside the cavitation itself. The problem they faced was overexposure of the particles added to the water (they were not visible since the vapour structure reflects much more light), so the velocity field inside the cavitation structure was not determined. The method applied in the present study, which allows also the flow measurements inside the vapour structure and the simultaneous acquisition of the shape of the cavitation structure, is a combination of PIV method, LIF (Laser Induced Fluorescence) technique and a use of two cameras. The technique is relatively new and was previously used for studies on the similar geometries and also on model pump runners (Friedrichs and Kosyna [7] and Bachert et al. [8]). The experiment performed and described in this paper concerns the evaluation of the velocity field, pressure distribution on the surface of the hydrofoil, the shape of the cavitation structures around a hydrofoil and the shedding frequencies of cavitation structures. The paper discusses an experimental and numerical study of unsteady phenomena of cavitating flow around two different hydrofoil configurations. In order to obtain the velocity distribution in the whole region of interest (also inside the cavitation structure) the PIV method was combined with the LIF technique. Instantaneous images of vapour structures were recorded using a CCD (Charged Coupled Device) camera. The vapour shedding frequencies were determined with use of high speed visualization. In the last decade various methods for numerical simulation of cavitating flow were developed. Most of the studies treat the two phase flow as a single vapour–liquid phase mixture flow. The evaporation and condensation can be modelled with different source terms that are usually derived from the Rayleigh–Plesset bubble dynamics equation. This approach was first made by Kubota et al. [9] who used the linear part in the Rayleigh–Plesset to equation to describe the evolution of bubble radius as a function of surrounding pressure. Different other cavitation models that included more complex relations between pressure and bubble radius were derived from the Rayleigh–Plesset equation – for example Schnerr and Sauer [10] and Frobenius [11], but they all included some quantities (like bubble number density and initial bubble diameter) that are impossible or very hard to determine. For example the recommended (estimated) value for bubble number density that has to be included in the mentioned models is 10^4 m^{-3} according to Kubota et al. [9], 10^8 m^{-3} according to Schnerr and Sauer [10] or to Frobenius et al. [11] and even 10^{12} m^{-3} according to Alajbegovic et al. [12].

Recently different authors proposed to consider a transport equation model for the void ratio, with vaporization/condensation source terms to control the mass transfer between the two phases (Singhal et al. [13], Merkle et al. [14], Kunz et al. [15], Senocak and Shvy [16] and Owis and Nayfeh [17]). This method has the advantage that it can take into account the time influence on the mass transfer phenomena through empirical laws for the source term. It also avoids using, hard to determine, quantities like bubble number density and initial bubble diameter. The other way to model cavitation process is by the so called barotropic state law that links the density of vapour–liquid mixture to the local static pressure. The model was proposed by Delannoy and Kueny [18] and later widely used by other (Coutier-Delgosha et al. [19], Hofmann et al. [20], Lohrberg et al. [21] and Song

and He [22]). The results obtained with the barotropic cavitation model show very good correlation to the experiments but the past simulations lacked in robustness of the numerical algorithms, which resulted in numerical instability and sometimes, poor convergence. Our past studies with this model also revealed that a lot of experience with adjustments to the function that links the density to the local pressure is needed to get plausible (or at least converged) results (Hofmann [23], Habr [24]). The commercial CFD code Fluent 6.1.18 was used for 3D transient simulations. A cavitation model, based on bubble dynamics equations, described in Singhal et al. [13] is included in the code and it was used to describe the unsteady behaviour of cavitation including the shedding of vapour structures. Since one of the aspects of the study was to test a commercial CFD code no changes to the software and default parameters, except a small (but important) modification of the turbulent model, were made.

2. Experimental set-up

Experiments were set up in a cavitation tunnel at the Laboratory for Turbomachinery and Fluid Power – Darmstadt University of Technology. Two simple hydrofoils were used. The basic geometry is a 50 mm wide, 107.9 mm long and 16 mm thick symmetric hydrofoil with circular leading edge and parallel walls. In order to obtain three-dimensional cavitation effects the basic geometry was modified by sweeping back the leading edge at an angle of 15 (Asymmetric Leading Edge hydrofoil – ALE15) and 25 degrees (ALE25) (Fig. 1). Additionally special hydrofoils were used for determining the pressure coefficient distribution on the surface of the hydrofoil (Fig. 6). The hydrofoil was inserted into the rectangular test section of a cavitation tunnel with closed circuit (Fig. 2) that enabled to change the system pressure and consequently the cavitation number. The test section is 500 mm long, 100 mm high and 50 mm wide.

The velocity in the reference plane upstream of the hydrofoil was held constant at 13 m/s ($Re = 1.38 \times 10^6$ based on the chord length) and verified by the LDA (Laser Doppler Anemometry) method. The turbulence intensity level upstream of the hydrofoil was derived from the LDA measurements and was 3%. The measurement of flow velocity was made with inductive flow meter Fischer & Porter D10D with uncertainty of 1% of the measured value.

Developed cavitating flow was observed at an incidence angle of 5° and at cavitation number of 2.3, which is defined as the difference between system and vapour pressure (at system temperature) divided by the dynamic pressure:

$$\sigma = \frac{p_\infty - p_\mathrm{v}(T_\infty)}{\rho \cdot v^2/2}. \tag{1}$$

The system pressure was measured with sensor JPB – Type 304 on each channel wall, 5 chord lengths upstream of the hydrofoil and then averaged. The temperature was measured with Jumo PT100 sensor. Considering the combination of inaccuracies of pressure, velocity and temperature measurements, the cavitation number could be determined within ± 0.04 of the measured value (Hofmann et al. [20]). The water used for the experiments was almost saturated with gasses (more then 50 mg of gas per liter of water) so that the effects of the tensile strength of the water were reduced to the maximal possible level. This condition is necessary since the variations in water quality can greatly influence the cavitation behaviour (as reported by Iwai and Li [25]).

Fig. 1. The ALE15 (left) and ALE25 (right) hydrofoils that were used for the experiments.

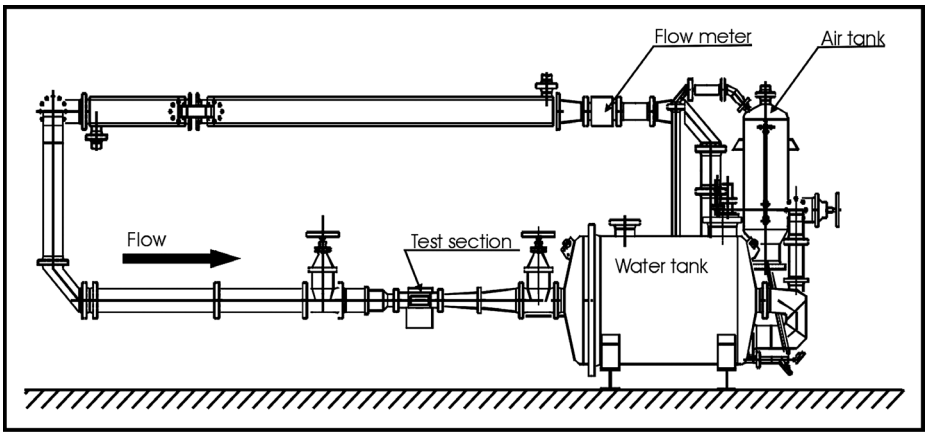

Fig. 2. Cavitation tunnel.

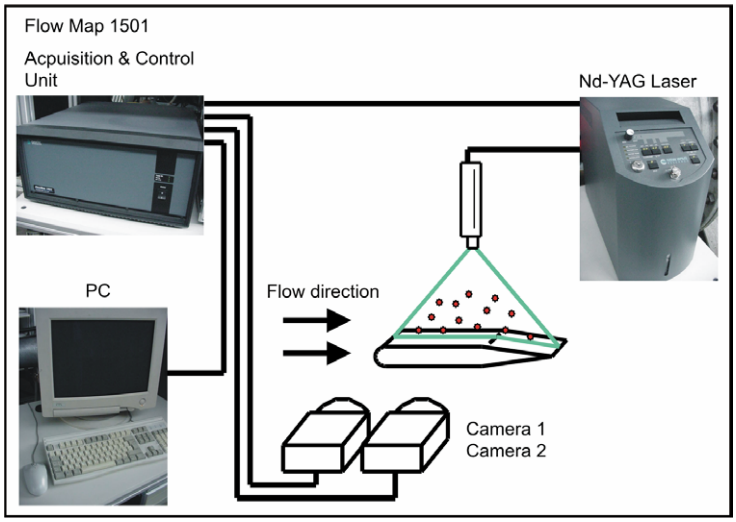

Fig. 3. Experimental set-up.

2.1. Experimental evaluation of cavitating flow

The shape and dynamics of cavitation structures and the velocity field around the hydrofoil were investigated. The combination of the PIV technique with LIF technique (Fig. 3) makes it possible to obtain the information about the velocity field outside and inside the cavitation pocket on the hydrofoil. The problem of using PIV in cavitating flow is the presence of an interface between the liquid and the vapour structures. The scattering of the laser light at the interface prevents the acquisition of usable images for the PIV analyses. A relatively new technique (Friedrichs and Kosyna [7] and Bachert et al. [8]) of combining the PIV method with the LIF technique to obtain the information on the velocity field outside and inside the vapour structure was used together with two CCD-cameras (Fig. 3) so that the location and extent of the instantaneous vapour zones was determined simultaneously with the corresponding velocity field.

For the PIV measurements, the region of interest extended over the hydrofoil (from 20 mm upstream of the leading edge to the curvature of the hydrofoil and from the surface of the hydrofoil it was 76 mm high) and was illuminated by a vertical laser light-sheet (Nd-YAG-Laser) approximately 1 mm thick and parallel to the flow direction. The position of the light sheet was 5 mm from the front wall (observation window), where the hydrofoil chord length is the smallest. Two CCD-cameras were installed with their optical axes oriented orthogonally to the light sheet. Special fluorescent tracer particles (PMMA-Rhodamin B, diameter is 1–20 μm) were added to the water for the PIV measurements. The particles receive light from the laser at a wavelength of 532 nm (green spectrum) and emit light at a wavelength of 590 nm (yellow spectrum). By fitting one of the two CCD-cameras with an appropriate light filter (that filters the visible light but lets the light in yellow spectrum trough) it

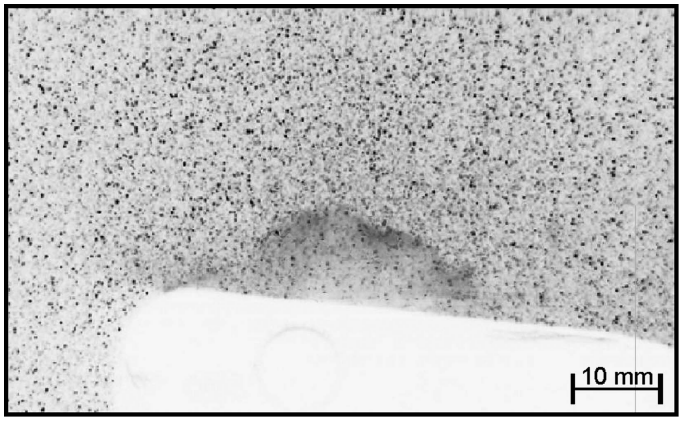

Fig. 4. Instantaneous image of tracer particles.

is possible to get suitable images of the tracer particles for the PIV analysis with the PIV-camera (the one with the filter) while the second camera takes an image in the whole spectrum of light and records the visible cavitation structure at the same time. Since one camera records only the light in the yellow spectrum, the cavitation structure is filtered out of that image and tracer particles inside it can also be detected. A typical image of tracer particles can be seen in Fig. 4.

The cavitation structure is almost entirely blended out of the image. Despite less particles are detected inside the cavity a velocity field could be determined if the position of the light sheet was close enough to the front observation window (5 mm). When the light sheet was positioned further away from the front wall the velocity field inside the cavity was very hard to determine because of the scattering of the light on vapour structures. Since the velocity was measured so close to the wall, it could have a significant effect on the measurements and later on simulation. The thickness of the boundary layer was derived with LDA method and was in the order of 1 mm. Also the influence of a gap between the hydrofoil and the front wall was minimised by the construction of the channel where the hydrofoil was pressed against and sealed to the front observation window.

The two cameras were triggered by the control unit of the PIV-system in combination with the laser shots with duration of 10 ns. For the PIV analyses 2 images with 30 μs time delay were recorded. Using the standard DANTEC software a cross correlation of the two images of tracer particles was made. The image size is 1152×858 pixel, equal to 95.7×76.6 mm (8.3×10^{-2} mm/Pixel in x-direction and 8.9×10^{-2} mm/Pixel in y-direction). A low-pass Gaussian sub-pixel interpolation was used for the determination of the correlation peak. The size of the interrogation area was 16×16 pixels; the overleaping was 50% leading to distance of approximately 0.65 mm between the vectors. About 35% of all vectors were rejected in the area where no flow is present (the part of an image where hydrofoil contour is present). Additionally about 2% of the remaining vectors were recognized as invalid "bad" vectors and were substituted. With the PIV analysis software, the field of flow velocities inside and outside the vapour zone was determined (and plotted e.g. in the form of a vectorplot). The dominant error in the PIV measurements is the bias introduced by the sub-pixel peak finding algorithm, which is in the order of 0.1 pixels, hence the average uncertainty of measured velocity using PIV-LIF technique was estimated to 2% (Laberteaux and Ceccio [5]).

The images of both cameras were recorded simultaneously. The result of the PIV analysis (vectorplot) was superposed to the conventional image of the cavitating zone taken by the second camera (Figs. 10 and 11). The information on the magnitude and the direction of the flow velocity and on the location, size and shape of the corresponding cavitation structure can be presented in one figure. A single image of this type gives information of the instantaneous characteristics of the unsteady cavitating flow. The displayed vectors were calculated in consideration of their neighbour-vectors.

The frequency of image capturing was 0.5 Hz. The velocity field was determined only from a side view, while the images of vapour structures were recorded from top view also (Fig. 5).

Sequence (made from characteristic single images) of cavitating flow around ALE25 hydrofoil from top view is presented in Fig. 5. The flow is from left to the right. A significant influence of swept leading edge can be seen. While the cavitation stays steady in the region where the hydrofoil is the longest, it has an obvious dynamical behaviour (periodically repeating separation of cavitation clouds) in the region where the hydrofoil is the shortest. Cavitation cloud is separated from the attached cavity. It then travels with the flow and collapses in a higher pressure region. The reason for the cloud separation is a significant back flow (re-entrant jet), which is generated at preceding cloud collapse. The reason for the difference in the behaviour of cavitation in the regions close to the front and close to the back wall is still unclear. A possible explanation can be seen from the distributions of c_p values on the surface of the hydrofoil (Fig. 16). The c_p distribution reveals a generally lower pressure region where the hydrofoil is the shortest. A possible influence of the swept leading edge on the decrease of c_p is a small variation in

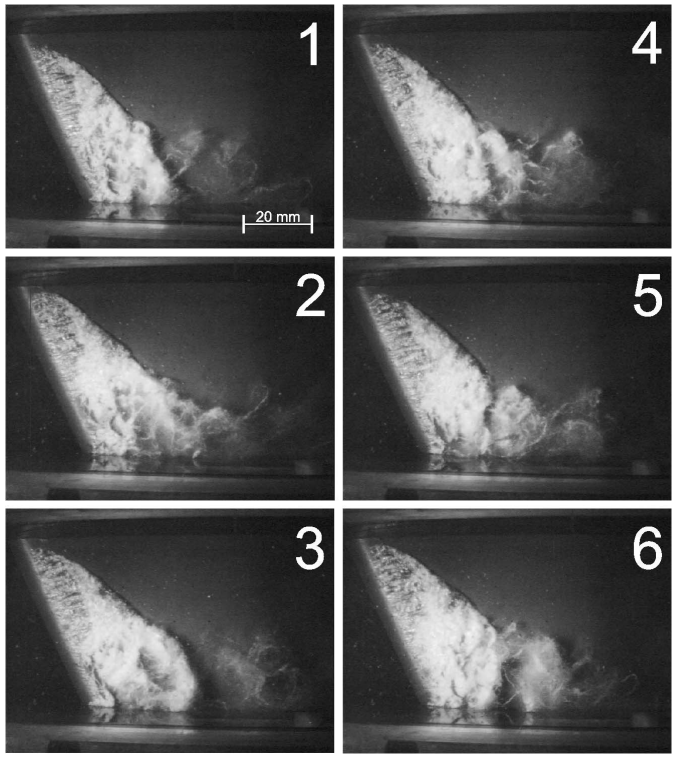

Fig. 5. Cavitation cloud separation on ALE25 hydrofoil at cavitation number $\sigma = 2.3$.

the flow direction towards the left side (looking in the main flow direction) as it approaches the hydrofoil (Bachert et al. [8]). The deviation of the flow generates a lower pressure region near the front wall (where the hydrofoil is the shortest), where the conditions for developed cavitating flow with cavitation cloud separation and re-entrant jet formation occur, while a steady attached cavitating zone is present in the region near the back wall where the hydrofoil is the longest. One other reason could also be the influence of the lateral walls of the channel. This was proven not to be so with the help of the simplified simulation where channel walls were not considered. The characteristic cloud separation occurred in the same region (where the hydrofoil is the shortest) and cavitation remained steady in the region where the hydrofoil is the longest.

Static pressure and consequently pressure coefficient on hydrofoil surface was measured. Special hydrofoils with 25 holes for pressure measurement were used. The position of the holes with diameter of 0.5 mm can be seen in Fig. 6. The average uncertainty of the pressure measurement was 1.5% of the measured value (Hofmann [23]).

3. Numerical simulation

Until now the simulation of the cavitating flow was only possible with special (in house made) CFD tools. One of the aspects of the study was to test capabilities of commercially available CFD code, hence program package Fluent 6.1.18 was used to calculate the cavitating flow. It is a 3-dimensional structured mesh code that solves a set of time dependant Reynolds-averaged Navier–Stokes equations (URANS) in a conservative form. The numerical model uses an implicit finite volume scheme, based on a SIMPLE algorithm (Patankar [26], Ferziger and Perić [27]), associated with multiphase and cavitation model. The SIMPLE algorithm needs to be modified in a similar way as for the case of highly compressible flows (Senocak and Shvy [16]). One of the most important features of the method is to reformulate the pressure correction equation to exhibit a convective-diffusive nature. In the cavitation model a convection equation with pressure dependent source terms (Eq. (6)), is solved to determine the density field. Because of this coupling the pressure correction equation needs to be reformulated although the model does not explicitly address the compressibility effects. This is achieved with the implementation of a pressure-velocity-density coupling scheme into the pressure correction equation. The scheme combines the incompressible and compressible formulations, to preserve the incompressibility of the liquid phase and to take into account the pressure-density dependency in the cavitating regions. In the present algorithm, the relation between density and pressure developed by Senocak and Shyy [16] is introduced to establish the pressure-velocity-density coupling. A 2nd order implicit temporal discretization was used. A 2nd order upwind differentiating

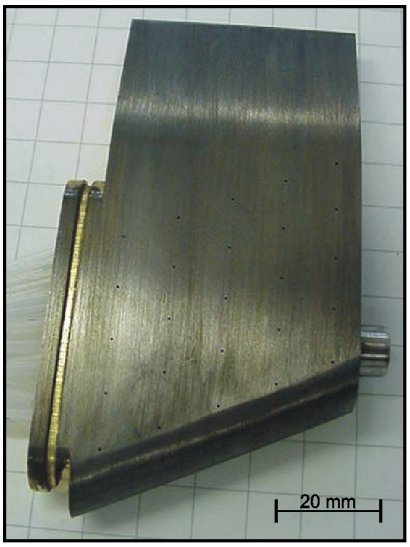

Fig. 6. ALE25 hydrofoil prepared for the measurement of static pressure.

scheme was used. A relatively high under-relaxation factor for the volume fraction (0.25), which does not influence the final solution but still allows a stabile simulation, was used.

3.1. Multiphase model

A single fluid (mixture phase) approach was used. The basic approach consists of using the standard (Navier–Stokes) viscous flow equations and a conventional turbulence model (RNG k–ε model). The mass (Eq. (4)) and momentum (Eq. (5)) conservation equations together with the transport equation (Eq. (6)) and the equations of the turbulence model form the set of equations from which the fluid density (which is a function of vapour mass fraction f_v) is computed. The ρ_m–f_v (mixture density–vapour mass fraction) relationship is:

$$\frac{1}{\rho_\mathrm{m}} = \frac{f_\mathrm{v}}{\rho_\mathrm{v}} + \frac{1 - f_\mathrm{v}}{\rho_\mathrm{l}}. \tag{2}$$

The volume fraction of the vapour phase (α_v) is related to of the mass fraction of the vapour phase with:

$$\alpha_\mathrm{v} = f_\mathrm{v} \frac{\rho_\mathrm{m}}{\rho_\mathrm{v}}. \tag{3}$$

The mass conservation equation for the mixture is:

$$\frac{\partial}{\partial t}(\rho_\mathrm{m}) + \nabla \cdot (\rho_\mathrm{m} \vec{v}_\mathrm{m}) = 0. \tag{4}$$

The momentum conservation equation for the mixture is:

$$\frac{\partial}{\partial t}(\rho_\mathrm{m} \vec{v}_\mathrm{m}) + \nabla \cdot (\rho_\mathrm{m} \vec{v}_\mathrm{m} \vec{v}_\mathrm{m}) = -\nabla p + \nabla \cdot \left[\mu_\mathrm{m} (\nabla \vec{v}_\mathrm{m} + \nabla \vec{v}_\mathrm{m}^\mathrm{T})\right] + \rho_\mathrm{m} \vec{g} + \vec{F}. \tag{5}$$

And the transport equation for the vapour is:

$$\frac{\partial}{\partial t}(\rho_\mathrm{m} f_\mathrm{v}) + \nabla \cdot (\rho_\mathrm{m} \vec{v}_\mathrm{m} f_\mathrm{v}) = R_\mathrm{e} - R_\mathrm{c}. \tag{6}$$

3.2. Cavitation model

Source terms R_e and R_c that are included in the transport equation define vapour generation (liquid evaporation) and vapour condensation, respectively. Source terms are functions of local flow conditions (static pressure, velocity) and fluid properties (liquid and vapour phase densities, saturation pressure and liquid vapour surface tension). The source terms are derived from the Rayleigh–Plesset equation, where high order terms and viscosity term have been left out. The derivation of the source terms can be found in Singhal et al. [13].

They are given by:

$$R_e = C_e \frac{\sqrt{k}}{\gamma} \rho_l \rho_v \sqrt{\frac{2}{3} \frac{p_v - p}{\rho_l}} (1 - f_v - f_g), \quad \text{when } p < p_v, \tag{7}$$

and by:

$$R_c = C_c \frac{\sqrt{k}}{\gamma} \rho_l \rho_l \cdot \sqrt{\frac{2}{3} \frac{p - p_v}{\rho_l}} f_v, \quad \text{when } p > p_v, \tag{8}$$

where C_e and C_c are empirical constants, k is the local kinetic energy, γ surface tension, f_v vapour mass fraction and f_g mass fraction of noncondensable (dissolved) gases. C_e and C_c were determined by comparing experimental and numerical results at different combinations of initial conditions and geometries, reported by Singhal et al. [13]; their values are 0.02 and 0.01 respectively.

3.3. Turbulence model

The RNG k–ε turbulence model was applied for solving the transport equations of the turbulent kinetic energy and its dissipation rate. The model itself is unable to correctly simulate the unsteady behaviour of cavitation. After an initial fluctuation of the cavity volume, the calculation leads to a quasi steady behaviour of the cavitation sheet, which becomes stabile. Also the overall length of the predicted cavity structure is about 50% too short compared to experimental results. The problem seems to lie in the overprediction of the turbulent viscosity in the region of cavity closure. The re-entrant jet formation, which is the main cause for the cavitation cloud separation, does not take place in this case. As reported by Reboud et al. [28] the problem seems to be related to the hypothesis of homogeneous flow approach – the no slip condition between the phases. The no slip condition behaves as an artificial increase of dissipation that has to be treated. In fact the premature disappearance of the back flow in the regions near the solid walls is common when using different turbulent models.

To improve the simulation a modification of the turbulent viscosity was applied as it was proposed and successfully proven by Reboud et al. [28]. In regions with higher vapour volume fractions (lower mixture densities) a modification of the RNG k–ε turbulence model was made by artificially reducing the turbulent viscosity of the mixture:

$$\mu_t = f(\rho) C_\mu \frac{k^2}{\varepsilon}, \tag{9}$$

$$f(\rho) = \rho_v + \frac{(\rho_m - \rho_v)^n}{(\rho_l - \rho_v)^{n-1}} \quad \text{where } n \gg 1. \tag{10}$$

This modification limits the turbulent viscosity in the region filled mainly by vapour phase and consequently allows the formation of a re-entrant jet and the cavitation cloud separation. Different values for exponent n were investigated. The most plausible results were obtained with values raging from $n = 7, \ldots, 15$. As recommended by Coutier-Delgosha et al. [19] $n = 10$ was eventually used.

4. Simulation

The computational domain stretched from 10 chord lengths in front of the hydrofoil to 10 chord lengths behind the hydrofoil. The cross sectional dimensions of the domain were the same as the test section dimensions (50 mm wide and 100 mm high). To check the influence of spatial and time discretization, a study of these parameters was made. Results are presented in Table 1.

When the mesh was fine enough, almost no influence of grid size was found. The discretization error of 0.5% was estimated. Time step size was more influential. The simulation diverged when time step $10^{-}4$ s or larger was used. It was determined that at least 100 time steps per shedding period must be used to avoid greater influence. Eventually C-type structured meshes with about 360 000 nodes (Fig. 7) and time step 2×10^{-5} s were used. Standard wall functions were applied, hence the y^+ value lies between 30 and 80.

The convergence criterion was determined by observing the evolution of different flow parameters (velocity magnitude at outlet, static pressure behind the hydrofoil) in the computational domain. The monitored flow parameters were always converged after the sum of the imbalance of the transport equations between iterations over all cells in the computational domain (residuals of the variables: pressure, velocity, turbulent kinetic energy, dissipation of turbulent kinetic energy and volume fraction) fell below $10^{-}3$ (after the error residuals drop by 3 orders of magnitude). After that, a number of different values (from $10^{-}3$ to 5×10^{-5}) for residuals were tested (Table 1), but no significant difference in the solution was found. Eventually a criterion for

Table 1
Results of spatial and time discretization influence and iteration cut-off influence study (ALE15 hydrofoil; the cavity length is measured 5 mm from the front wall)

Time step (s)	Grid size	Residuals	Shedding frequency (Hz)	Cavity length (mm)
5×10^{-5}	~360 000	5×10^{-4}	227	54
1×10^{-4}	~360 000	5×10^{-4}	NOT STABIL	NOT STABIL
2×10^{-5}	~180 000	5×10^{-4}	244	53
2×10^{-5}	~360 000	5×10^{-4}	238	57
2×10^{-5}	~720 000	5×10^{-4}	236	58
2×10^{-5}	~360 000	1×10^{-3}	233	55
2×10^{-5}	~360 000	5×10^{-5}	238	57

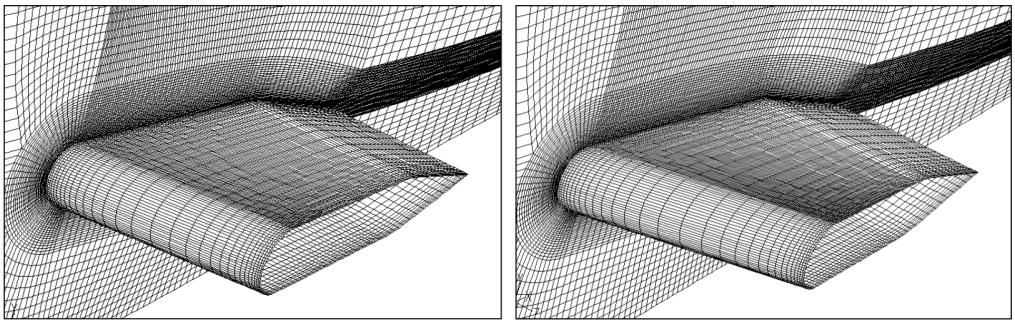

Fig. 7. Computational domain around ALE15 (left) and ALE25 (right) hydrofoils (the front wall is not represented).

the converged time step solution was set to the point when the residuals fell below 5×10^{-4}. Approximately 40 iterations per time step were needed to obtain a converged solution. The iteration error of 0.05% was estimated.

Conditions applied for the simulation were the following:

- Boundary condition: Imposed velocity at inlet and static pressure at outlet. The channel walls are also considered so that the possible wall effects are taken into account.
- Initial transient treatment: A low velocity was initially applied to the flow field, for which no vapour appears. The velocity was then increased until the desired operating point (cavitation number) was reached. The turbulence level at inlet boundary condition was set to 3%.
- Because the experimental cavitation number is based on upstream pressure, the losses generated in the test section had to be taken into account in the calculation of the numerical cavitation number. The desired operating point (cavitation number) was reached by comparison of the experimental and numerical upstream pressure. Since the pressure is imposed at the outlet it can slightly oscillate at the inlet into the domain, hence the pressure used to calculate the numerical upstream cavitation number was time averaged. The upstream cavitation number was the same for the experiments and for the simulation (defined at the same point in the domain (5 chord lengths upstream of the hydrofoil); $\sigma = 2.3$). The turbulence level at outlet boundary condition was set to 3%.
- Different time step values were tested; eventually time step 2×10^{-5} s was used.

Although vapour–fluid mixture flow can reach sound speed at relatively low velocities, compressibility effects were neglected since Fluent does not allow compressible multiphase flow computation. It was shown by Coutier-Delgosha et al. [19] that plausible results can be obtained without consideration of compressibility effects if a modification of turbulent viscosity (Section 3.3) is applied. Despite the compressibility effects were neglected is the simulation capable to predict many features of the developed cavitating flow (like cloud separation and re-entrant jet) but for example cannot predict the shock waves that are emitted at cavitation cloud collapse.

The values $\rho_l = 998.2$ kg/m^3, $\rho_v = 0.554$ kg/m^3, $\mu_l = 10^{-3}$ Pas, $\mu_v = 1.34 \times 10^{-5}$ Pas, $\gamma = 0.0717$ N/m for liquid and vapour density, liquid and vapour dynamical viscosity and surface tension respectively, were used for the simulation. The gas content of the water was measured during the experiments and the value was given as an input into the simulation ($f_g = 5 \times 10^{-5}$).

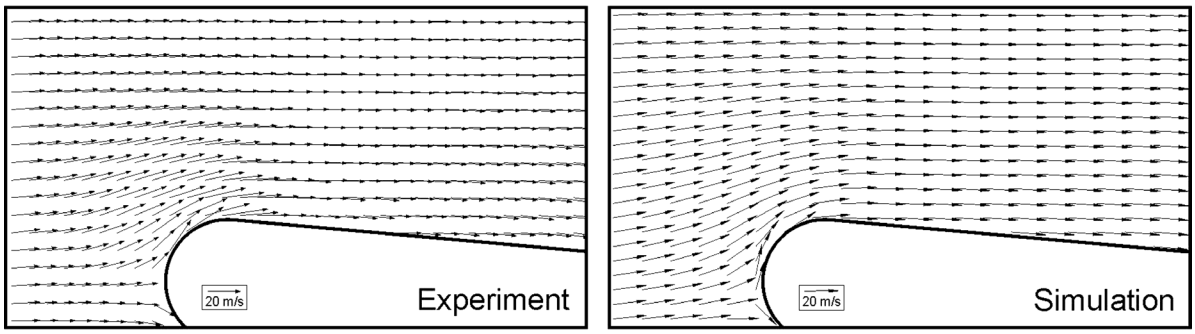

Fig. 8. Experimentally measured (left) and numerically predicted velocity field around the hydrofoil for noncavitating condition.

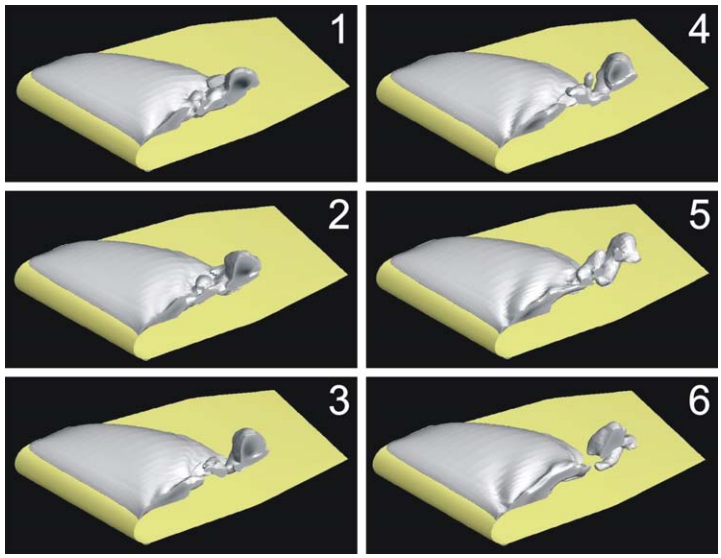

Fig. 9. Numerically predicted time evolution of cavitation structure on ALE25 hydrofoil at $\sigma = 2.3$.

5. Comparison between experimental results and simulation

Since the geometry of the hydrofoil is not conventional a steady simulation of the noncavitating flow (upstream pressure $p_\infty = 5.1$ bar, $v = 13$ m/s; $\sigma = 6$) was made to get the idea of the flow conditions. Comparison between experimental results of velocity measurements and numerical simulation on ALE15 hydrofoil is presented in Fig. 8.

We can see that the rapid transition to the plane part of the hydrofoil does not cause the separation of the flow when the incidence angle is small enough (5°).

The transition of the simulated cavitation structures is presented in Fig. 9.

Sequence of images of numerical simulation of cavitation around ALE25 hydrofoil is presented. Isosurfaces of 10% vapour volume fractions are shown (the value of 10% vapour volume fraction was chosen on the basis of previous experience that shows that it relates best to the real cavity shapes) (Okita and Kajishima [29]). The time delay between the images is 0.6 ms. As in the experiment (Fig. 5) a steady attached cavitation can be seen in the region where the hydrofoil is the longest. The cloud separation occurs only in the region where the hydrofoil is the shortest. The cavitation structure firstly grows. The re-entrant jet (not presented in the sequence) causes the cavitation cloud separation in the region near the front wall. The separated cloud travels with the flow and implodes downstream in a higher pressure region. The implosion of the cloud forms a new re-entrant jet that causes the next cavitation cloud separation.

Experimentally determined instantaneous velocity fields and images of cavitation structures together with predictions of numerical simulation are shown in Fig. 10. The magnification of the situation in the zone where cavitation structure is present is shown in Fig. 11 (detail A and B). The position of the light sheet was 5 mm from the front wall (where the hydrofoil is the

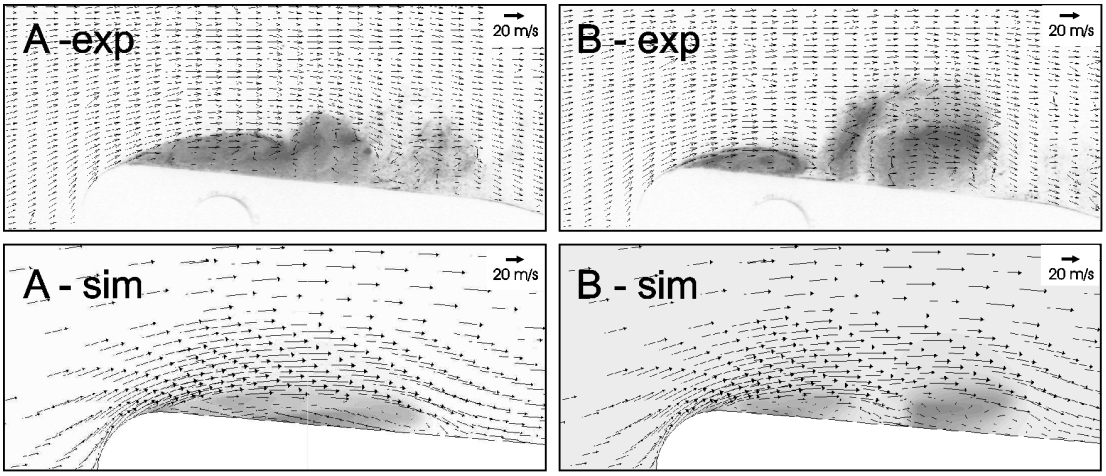

Fig. 10. Experimentally determined and numerically predicted instantaneous flow and vapour field on ALE25 hydrofoil at $\sigma = 2.3$. The position of the plane of the presented velocity and vapour field is 5 mm from the front wall.

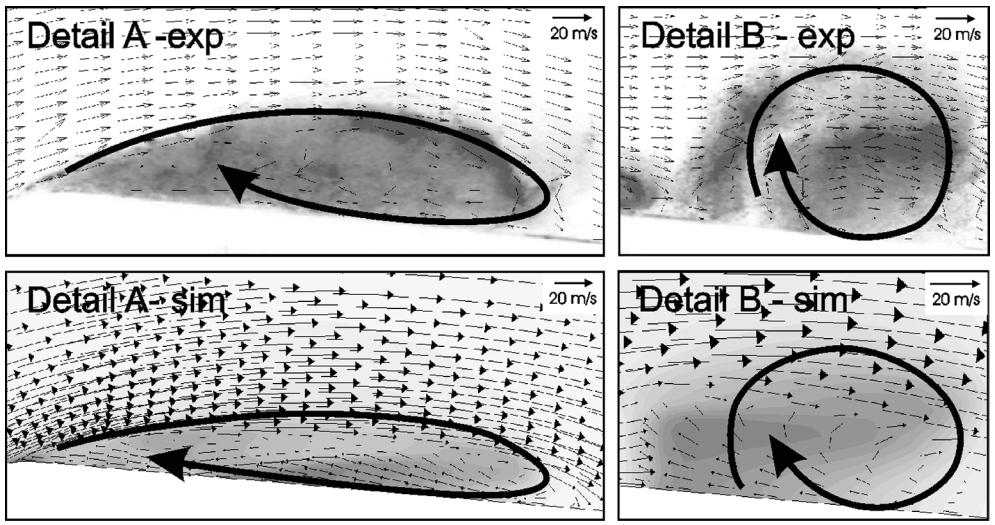

Fig. 11. Magnified look at experimentally determined and numerically predicted instantaneous flow and vapour field on ALE25 hydrofoil at $\sigma = 2.3$. The position of the plane of the presented velocity and vapour field is 5 mm from the front wall.

shortest); the results of numerical simulation are obtained at the same position on the hydrofoil. The arrow in the magnified images (Fig. 11) denotes the main flow direction of the re-entrant jet.

The top two images are results of PIV-LIF measurement while the bottom two correspond to the predictions of numerical simulation. The left two images (A) show the instantaneous situation just before the cavitation cloud separation. One can see a significant back flow inside the cavity near the surface. Experimental results show that it is present from the cavity closure up to 80% of the mean cavity length upstream. The back flow (re-entrant jet) phenomenon is correctly predicted in simulation. The right two images (B) correspond to the situation after the cavitation cloud separation. A forming re-entrant jet (a vortex rotating in a clockwise manner) can be seen downstream of the separated cavitation cloud. The forming re-entrant jet can also be seen in simulation prediction (bottom right images (B) in Fig. 10 and 11). The maximal measured backflow velocity was -13.2 m/s. The maximal simulated backflow velocity was -14.3 m/s.

A quantitative comparison of the results was made. The mean velocity fields were determined by averaging 50 instantaneous PIV-LIV data sets. A mean velocity convergence study was made (Fig. 12). The difference between mean velocity of N and $N - 1$ images was calculated.

The convergence study revealed that the uncertainty of the magnitude of mean velocity is less than 1% when more than 40 data sets ($N > 40$) are averaged.

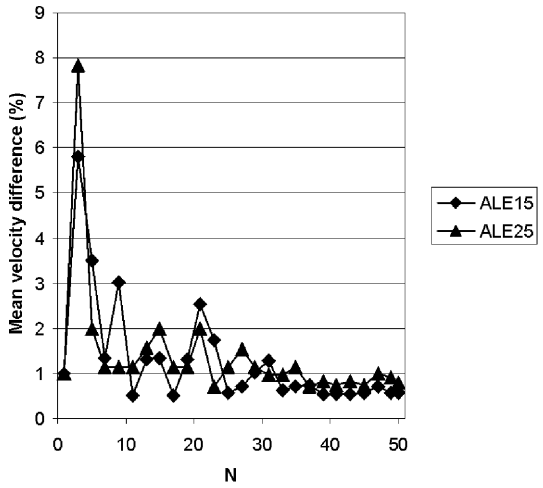

Fig. 12. Convergence diagram of mean velocity magnitude for ALE15 and ALE25 hydrofoils.

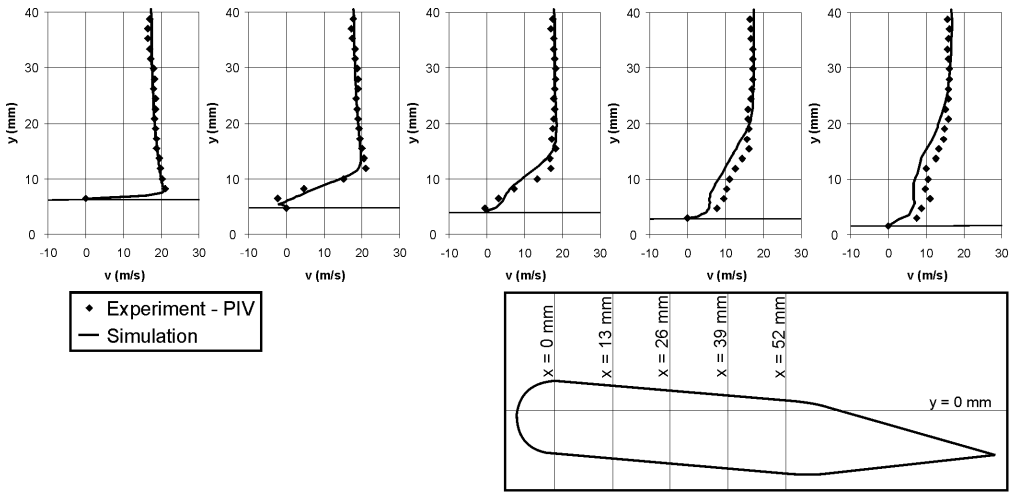

Fig. 13. Mean experimental and numerical velocity profiles (x-direction) for ALE15 hydrofoil.

Comparison of the experimental and numerical velocity profiles in the x (flow) direction on hydrofoils ALE15 and ALE25 are shown in Figs. 13 and 14, respectively. The velocity profiles at 5 positions on a plane 5 mm from the channel wall (where the hydrofoil is the shortest) are compared. The bold horizontal lines in the diagrams represent the position of the hydrofoil's surface.

We can see that the velocity profiles in the planes $x = 26$ mm, $x = 39$ mm and $x = 52$ mm feature unusually gradual velocity decrease as we move towards the hydrofoil surface. The reason probably lies in the fact that the cavitation structure acts as an obstacle – the velocity decreases slower, as it does in noncavitating condition, when we move towards the surface of the hydrofoil. The other possible reason for the more gradual decrease of the velocity near the surface is the presence of the vortices left over from the collapsed cavitation clouds, which can only be seen in instantaneous images of the velocity field (Figs. 10 and 11).

It can be seen that the numerical simulation agrees well with experimental results. The velocity profiles on planes $x = 0$ mm and $x = 13$ mm are correctly predicted, while the numerically predicted velocities at the cavitation closure and behind it (planes $x = 26$ mm, $x = 39$ mm and $x = 52$ mm) show greater discrepancies. One reason for the discrepancy between the experimental and numerical results could be that a single fluid approach with no slip condition between the phases was used and that the simulated vapour field offers more resistance to the flow as the real one. The problem could maybe be solved if a two fluid multiphase model would be used (Alajbegovic et al. [12]). By solving mass and momentum conservation equations for each phase and considering the slip between the phases a more accurate simulation could probably be achieved, but a considerably

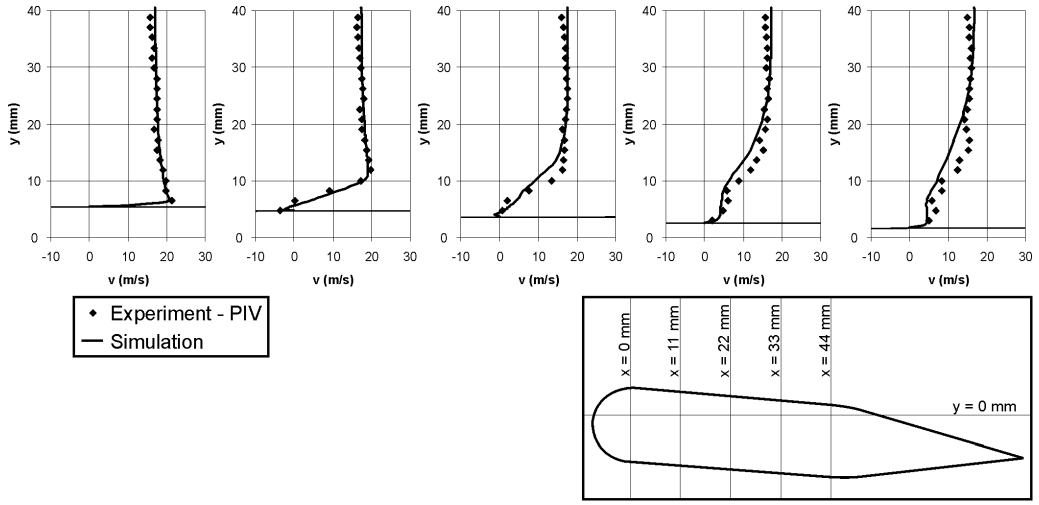

Fig. 14. Mean experimental and numerical velocity profiles (x-direction) for ALE25 hydrofoil.

longer computational would then be expected. The other possible reason for the difference is probably the turbulence model, which can produce artificially high turbulent kinetic energy and causes premature dissipation of the vortices. Nevertheless the numerical predicted velocities show the same trend as the experimentally obtained ones. The back flow (seen on plane $x = 13$ mm) can be seen in both numerical and experimental results, although the numerical simulation slightly underestimates its magnitude and thickness. The velocity further away from the hydrofoil surface is correctly predicted all along the hydrofoil.

The numerical simulation of cavitating flow around ALE25 hydrofoil produced similar results. The velocities are well predicted on planes $x = 0$ mm and $x = 11$ mm. The magnitude and thickness of backflow on plane $x = 11$ mm agrees almost perfectly with experimental results. Similar to the ALE15 simulation the velocities on planes $x = 22$ mm, $x = 33$ mm and $x = 44$ mm show greater discrepancies, but the trends are similar.

Results of numerical simulation and experiment were compared for y direction (normal to the flow direction) (Fig. 15). The values at 4 y levels in a plane 5 mm from the channel wall (where the hydrofoil is the shortest) are shown for ALE15 hydrofoil (left) and ALE25 hydrofoil (right).

One can see that the simulation relatively correctly predicts the velocity magnitude in y direction. A significant increase of the velocity in the y direction can be seen as the flow approaches the hydrofoil leading edge. The effect is more obvious in the vicinity of the hydrofoil (plane $y = 0$ mm; bottom two diagrams). The maximal y-velocity is reached approximately at the point of transition from the circular leading edge to the plane surface of the hydrofoil (at $x = 20$ mm for the ALE15 hydrofoil and $x = 30$ mm for ALE25 hydrofoil). The numerical simulation and experimental measurements agree well in the significant decrease in y-velocity on a plane near the hydrofoil surface ($y = 0$ mm). Behind the position of transition from circular to plane part of the hydrofoil on the planes further away from the surface ($y = 10$ mm and $y = 15$ mm) of the hydrofoil the experimentally determined y-velocities decrease faster than simulated ones. The reason for the discrepancy is probably the turbulence model which can produce artificially high turbulent kinetic energy that does not allow vortices to occur, hence the decrease rate of the y-velocity is smaller in the case of simulation as in the experiment (the simulated and experimental y-velocities agree well inside the cavitation zone ($y = 0$ mm) since the turbulence model is corrected by the modification of turbulent viscosity in region of lower densities). Since the hydrofoil is mounted at an incidence angle of 5° the y-velocity approaches a value a bit less than 0 as it flows past the hydrofoil.

The average discrepancy between experimental measurements and simulation results for the x and y velocity was estimated to less than 10%.

The experimental and numerically predicted time averaged distributions of pressure coefficient $c_p = (p - p_{ref})/(1/2\rho v^2)$ (measured pressure upstream of the hydrofoil was chosen for reference pressure – $p_{ref} = 197\,200$ Pa) are shown in Fig. 16. The measurements were done at 25 positions on the hydrofoil surface.

The diagrams show the results of experimental measurements and numerical predictions of pressure coefficient on the surfaces of ALE15 (left) and ALE25 (right) hydrofoils. The trends of experimentally measured and numerically predicted c_p values are correct. Greater discrepancies can be seen for the values near the cavity closure region (where the cloud separation occurs) (positions 3, 8, 13, 18 and 23) and near the leading edge (positions 1, 6, 11, 16 and 21). The greater discrepancies in these regions are expected since the pressure gradients and fluctuations are larger and also the uncertainty of the pressure measurements is greater in the lower pressure region. On the other hand results agree better in the flow where no cavitation was present

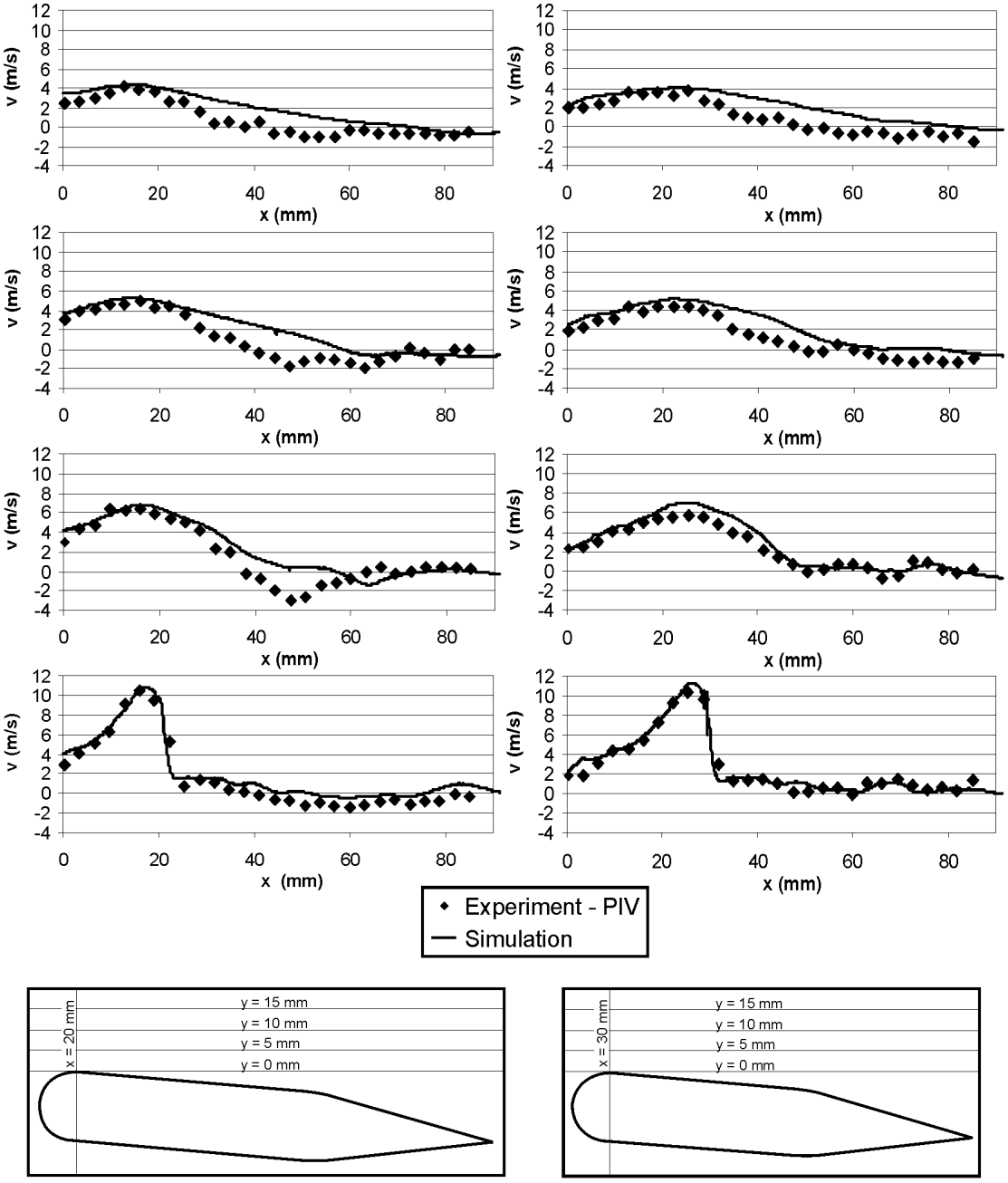

Fig. 15. Mean experimental and numerical velocity profiles (y-direction) for ALE15 and ALE25 hydrofoil.

– downstream of the cavity closure (positions 5, 10, 15, 20 and 25). One can see that two different trends of c_p distribution as we move away from the leading edge. In the first case c_p is low on the first two taps and then increases dramatically on the third tap (looking for example ALE15 hydrofoil (left) taps 1, 2 (lower c_p), 3 (rapid increase), 4, and 5 (higher c_p)). This situation is characteristic for the region where the hydrofoil is the shortest – where the cavitation cloud separation occurs. The other trend is similar, but the swift increase in c_p occurs already on the second tap (looking for example ALE15 hydrofoil taps 21 (lower c_p), 22 (rapid increase), 23, 24, and 25 (higher c_p)). This trend is characteristic for the region where hydrofoil is the longest – with attached cavitation with no cloud separation. The longer region with lower c_p (the first trend) is probably caused by the slight variation in the flow direction towards the left side in the flow direction (towards the back wall – where the hydrofoil is the

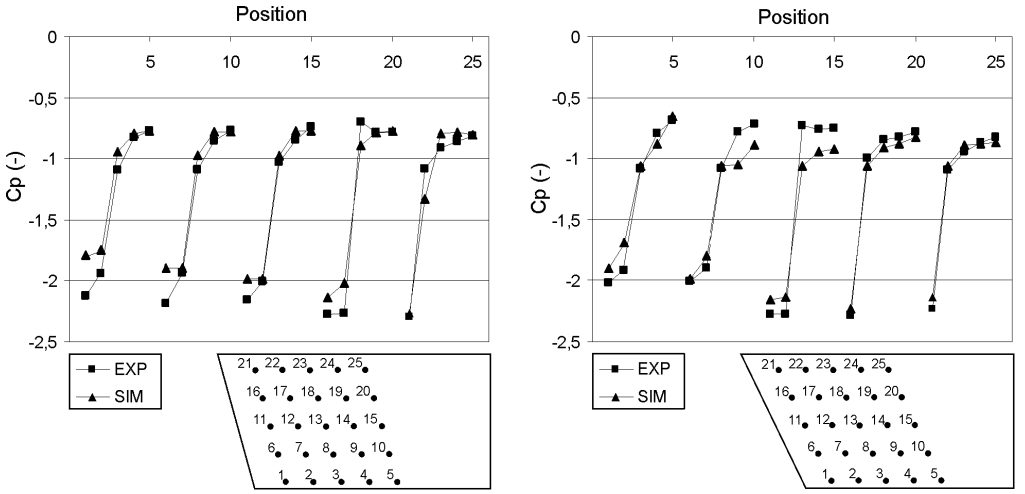

Fig. 16. Experimentally determined and numerically predicted values of pressure coefficient for ALE15 (left) and ALE25 (right) hydrofoils.

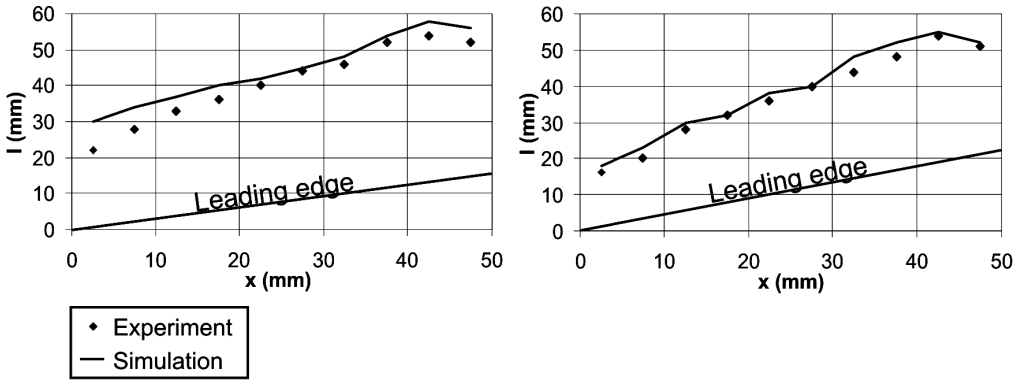

Fig. 17. Experimentally determined and numerically predicted cavitation structure shape for ALE15 (left) and ALE25 (right) hydrofoils.

longest) as it approaches the hydrofoil (Bachert et al. [8]). The deviation of the flow to the left side (towards the back wall – where the hydrofoil is the longest) causes a lower pressure region near the front wall (where the hydrofoil is the shortest). This way conditions (lower local pressure – lower local c_p) for a developed cavitating flow with cavitation cloud separation occur in this region, while a steady cavitating zone (attached cavitation) is present in the region where the hydrofoil is the longest (in the region with higher local pressure – higher local c_p) (Knapp et al. [30]). One can also observe that the region of the lower c_p is smaller for the ALE25 hydrofoil, which corresponds well to the cavitation type above the hydrofoil – the region of cavitation cloud separation is smaller for the ALE25 hydrofoil as for the ALE15 hydrofoil.

The average discrepancy between experimental measurements of c_p and numerical prediction was estimated to less than 10%.

The comparison between experimentally measured and numerically predicted mean cavity length is given in Fig. 17. The determination of the boundary of the cavity is a relatively inaccurate and difficult task.

Cavitation structures are characterized by a high value of gray level (bright region) in the recorded image. The boundary of the cavitation structure in each image was considered to be the isoline of a certain gray level (230 ($\sim$ 90% brightness); the pixles in the image in 8 bit resolution can occupy values from 0 (black) to 255 (white)). A time averaged cavity shape was determined by averaging the cavitation structure boundary data from each image.

In the simulation a common principle was used. An isoline of 10% vapour volume fraction (90% liquid volume fraction) at a certain time step was considered to be the boundary of the cavitation structure. The mean cavity shape was calculated by averaging the cavitation structure boundary data from each time step. The method is not very accurate and a lot of adjustments can be made to get plausible results (setting the boundary gray level for experimental and vapour volume fraction value for numerical results), hence the value of the presented results is mainly in the correct trend that is shown by numerical simulation rather than the correct quantitative comparison to the experiment.

The flow is from the bottom up. The left diagram shows the situation for the case of the ALE15 hydrofoil and the right the case of the ALE25 hydrofoil. Both diagrams show the correct trend of numerically predicted cavity length. Greater discrepancy can be seen on the left edge of ALE15 hydrofoil where the numerically predicted cavity length is overestimated.

The average discrepancy between simulation and experimentally measured cavitation structure length was estimated to less than 7%.

The numerical simulation gives us a possibility to easily determine cavitation cloud shedding frequencies. The experimental determination of shedding frequencies on present geometries was made using high speed visualization. A CCD camera that records 3600 frames per second was used. The experimental shedding frequencies were determined by a Fast-Fourier-Transform of the gray level values in the region of interest of the recorded images. For the ALE15 hydrofoil the shedding frequency was 302 ± 36 Hz and for the ALE25 hydrofoil 330 ± 62 Hz. The present numerical simulation sets the shedding frequency at 238 Hz for ALE15 hydrofoil and 262 Hz for ALE25 hydrofoil. The numerical shedding frequencies are not perfectly constant. They were deducted from 15 cycles and vary $\pm 15\%$ from the mean value. We can see that the simulation underestimates the shedding frequency, but we have to keep in mind that this is a particularly difficult phenomenon to simulate and that the simulation result can be considered plausible if the experimental and numerical shedding frequencies lie in the same order of magnitude. The reason for the discrepancy could lie in the fact that the whole test rig influences flow around the hydrofoil but only small section of it is included in computational domain.

6. Conclusions

Experimental and numerical investigations of different cavitating flow conditions on two different hydrofoils were performed. A relatively new experimental technique where PIV method is combined with LIF method was used for the determination of the velocity field in the liquid phase around the cavitating hydrofoil. The use of additional camera made it possible to determine the instantaneous cavitation structure shape and the corresponding velocity field inside and outside the cavitation structure. Using special hydrofoils the distribution of pressure coefficient on the surface of the hydrofoils was determined. The shedding frequencies of the cavitation structures were determined with high speed visualization.

The commercial CFD program – Fluent 6.1.18 was used for the simulation of cavitation. The disadvantage of using a commercial package is limited access to the code and therefore fewer possibilities for improvement of the simulation. For example the code does not allow the use of compressible flow computation with combination with multiphase flow. Despite an assumption of incompressible flow, results of numerical simulation show good correlation with experimental values if the turbulent viscosity is modified by an empirical relation to take into account the effect of liquid–vapour mixture on turbulence. The velocity field inside and outside of the vapour cavity is well simulated. As in the experiment, a significant backflow near the surface is predicted in the simulation. The numerically predicted pressure coefficient distribution agrees qualitatively well with the experimental results, but some quantitative discrepancies can be seen. The numerically predicted cavity length agrees with experimental results, although greater discrepancies can be found at certain positions. The simulated shedding frequencies are generally lower than experimentally determined but the discrepancies are still small enough that the results are plausible. It was generally found that the simulation is capable to predict many of the cavitating flow characteristic with considerable accuracy. The greatest discrepancies were always found in the region of transition from vapour to the liquid phase (behind the cavity closure), where the flow dynamics was high. The next step is to experimentally determine the velocity field in a plane parallel to the hydrofoil wall (at a distance of approximately 1–2 mm).

A challenge is also to reduce the computational time, which exceeded 300 hours for 3D simulations on a Pentium IV – 2.4 GHz processor (see Frobenius et al. [11]).

The presented experimental results are well suited for evaluation and calibration of different cavitation models and for verification of numerical results. The commercial CFD code Fluent proved to be a valuable tool for prediction of cavitating flow although it is questionable if simulations with very long computational time are already suitable for industrial applications.

References

[1] B. Sirok, M. Dular, M. Novak, M. Hocevar, B. Stoffel, G. Ludwig, B. Bachert, The influence of cavitation structures on the erosion of a symmetrical hydrofoil in a cavitation tunnel, J. Mech. Engrg. 48 (7) (2002) (Ljubljana, Slovenia).
[2] B. Stutz, J.L. Reboud, Experiment on unsteady cavitation, Exp. Fluids 22 (1997) 191–198.
[3] B. Stutz, J.L. Reboud, Measurements within unsteady cavitation, Exp. Fluids 29 (2000) 545–552.
[4] Y. Zhang, S. Gopalan, J. Katz, On the flow structure and turbulence in the closure region of attached cavitation, in: 22nd ONR Symp. on Naval Hydrodynamics, 1998, pp. 227–238.
[5] K.R. Laberteaux, S.L. Ceccio, Partial cavity flows. Part 1. Cavities forming on models without spanwise variation, J. Fluid Mech. 431 (2001) 1–41.

[6] K.R. Laberteaux, S.L. Ceccio, Partial cavity flows. Part 2. Cavities forming on test objects with spanwise variation, J. Fluid Mech. 431 (2001) 43–63.
[7] J. Friedrichs, G. Kosyna, Unsteady PIV flow field analysis of a centrifugal pump impeller under rotating cavitation, in: Proceedings of the Fifth International Symposium on Cavitation, Osaka, Japan, 2003.
[8] R. Bachert, B. Stoffel, R. Schilling, M. Frobenius, Three-dimensional, unsteady cavitation effects on a single hydrofoil and in a radial pump – measurements and numerical simulations; Part one: Experiments, in: Proceedings of the Fifth International Symposium on Cavitation, Osaka, Japan, 2003.
[9] A. Kubota, K. Hiroharu, H. Yamaguchi, A new modelling of cavitating flows, a numerical study of unsteady cavitation on a hydrofoil section, J. Fluid Mech. 240 (1992) 59–96.
[10] G.H. Schnerr, J. Sauer, Physical and numerical modelling of unsteady cavitation dynamics, in: 4th International Conference on Multyphase Flow, ICMF-2001,New Orleans, USA, 2001.
[11] M. Frobenius, R. Schilling, R. Bachert, B. Stoffel, Three-dimensional, unsteady cavitation effects on a single hydrofoil and in a radial pump – measurements and numerical simulations, Part two: Numerical simulation, in: Proceedings of the Fifth International Symposium on Cavitation, Osaka, Japan, 2003.
[12] A. Alajbegovic, H.A. Groger, H. Philipp, Calculation of transient cavitation in nozzle using the two-fluid model, in: 12th Annual Conference on Liquid Atomization and Spray Systems, Indianapolis, IN, USA, 1999.
[13] A.K. Singhal, H. Li, M.M. Atahavale, Y. Jiang, Mathematical basis and validation of the full cavitation model, J. Fluids Engrg. 124 (2002) 617–624.
[14] R. Kunz, D. Boger, T. Chyczewski, D. Stinebring, H. Gibeling, Multi-phase CFD analysis of natural and ventilated cavitation about submerged bodies, ASME FEDSM99-7364, SAN Francisco, 1999.
[15] C.L. Merkle, J. Feng, P.E.O. Buelow, Computational modeling of the dynamics of sheet cavitation, in: 3rd Int. Symp. on Cavitation, Grenoble, France, 1998.
[16] I. Senocak, I.W. Shvy, A pressure-based method for turbulent cavitating flow simulations, J. Comput. Phys. 176 (2002) 363–383.
[17] F.M. Owis, A.H. Nayfeh, Numerical simulation of 3-D incompressible, multi-phase flows over cavitating projectiles, Eur. J. Mech. B Fluids 23 (2004) 339–351.
[18] Y. Delannoy, J.L. Kueny, Two phase flow approach in unsteady cavitation modelling, in: Cavitation and Multiphase Flow Forum, ASME-FED, vol. 98, 1990, pp. 153–158.
[19] O. Coutier-Delgosha, R. Fortes-Patella, J.L. Reboud, Evaluation of turbulence model influence on the numerical simulations on unsteady cavitation, J. Fluids Engrg. 125 (2003) 38–45.
[20] M. Hofmann, H. Lohrberg, G. Ludwig, B. Stoffel B, J.L. Reboud, R. Fortes-Patella, Numerical and experimental investigations on the self – oscillating behaviour of cloud cavitation – Part 1: Visualisation, in: Proceedings of the 3rd ASME/JSME Joint Fluids Engineering Conference, San Francisco, CA, 1999.
[21] H. Lohrberg, B. Stoffel, R. Fortes-Patella, J.L. Reboud, Numerical and experimental investigations on the cavitation flow in cascade of hydrofoils, Exp. Fluids 33 (2002) 578–586.
[22] C.C. S Song, J. He, Numerical simulation of cavitating flows by single-phase flow approach, in: 3rd International Symposium on Cavitation, Grenoble, France, 1998, pp. 295–300.
[23] M. Hofmann, Ein Beitrag zur verminderung des erosiven Potentials kavitierender Stoemungen – PhD Thesis, Technishe Univesitaet Darmstadt, Darmstadt, 2001.
[24] K. Habr, Gekoppelte Simulation hydraulischer Gesamtsysteme unter Einbeziehung von CFD, PhD Thesis, Technishe Univesitaet Darmstadt, Darmstadt, 2001.
[25] Y. Iwai, S. Li, Cavitation erosion in waters having different surface tensions, Wear 254 (2003) 1–9.
[26] S.V. Patankar, Numerical Heat and Fluid Flow, Hemisphere, New York, 1980.
[27] J.H. Ferziger, M. Perić, Computational Methods for Fluid Dynamics, second ed., Springer, 1999.
[28] J.L. Reboud, B. Stutz, O. Coutier, Two-phase flow structure of cavitation: experiment and modelling of unsteady effects, in: Third International Symposium on Cavitation, Grenoble, France, 1998.
[29] K. Okita, T. Kajishima, Three-Dimensional Computation of Unsteady Cavitating Flow in a Cascade, in: The 9th of International Symposium on Transport Phenomena and Dynamics of Rotating Machinery Honolulu, Hawaii, 2002.
[30] R.T. Knapp, J.W. Daily, F.G. Hammitt, Cavitation, McGraw-Hill, London, 1970.